



3D map creation using crowdsourced GNSS data

Terence Lines, Anahid Basiri*

School of Geographical and Earth Sciences, The University of Glasgow, United Kingdom

A B S T R A C T

3D maps are increasingly useful for many applications such as drone navigation, emergency services, and urban planning. However, creating 3D maps and keeping them up-to-date using existing technologies, such as laser scanners, is expensive. This paper proposes and implements a novel approach to generate 2.5D (otherwise known as 3D level-of-detail (LOD) 1) maps for free using Global Navigation Satellite Systems (GNSS) signals, which are globally available and are blocked only by obstacles between the satellites and the receivers. This enables us to find the patterns of GNSS signal availability and create 3D maps. The paper applies algorithms to GNSS signal strength patterns based on a boot-strapped technique that iteratively trains the signal classifiers while generating the map. Results of the proposed technique demonstrate the ability to create 3D maps using automatically processed GNSS data. The results show that the third dimension, i.e. height of the buildings, can be estimated with below 5 metre accuracy, which is the benchmark recommended by the CityGML standard.

1. Introduction

3D maps are increasingly used in a number of applications, such as urban analytics and decision support systems (Biljecki et al., 2015; Döllner et al., 2006; Lin et al., 2009), several location-based services including navigation (Groves et al., 2012; Verbree & Zlatanova, 2007), autonomous vehicles (Levinson et al., 2011), path planning, map-matching for more reliable obstacle avoidance within drone navigation (Floreano & Wood, 2015), and the safety requirements of some emergency services (Kolbe, Gröger, & Plümer, 2008; Pu & Zlatanova, 2005). However, there are still challenges in creating and keeping them up-to-date. Existing specialist technologies for creating these maps, including airborne photogrammetry (Suveg & Vosselman, 2004) and airborne and ground-based laser scanning (Baltsavias, 1999; Pu & Vosselman, 2006) are relatively expensive. These costs are not one-off; they must be repeated regularly to keep maps up-to-date.

Alternative low-cost approaches automate the process of using localised knowledge through data-mining of administrative data (Biljecki, Ledoux, & Stoter, 2017; Yin, Wonka, & Razdan, 2008) or Volunteered Geographic Information (VGI) (Goetz, 2013). However, data-mining is limited by the coverage and temporal accuracy of the data source, and the quality of VGI generated maps cannot be taken for granted (Fan et al., 2014; Salk et al., 2016). Computer vision techniques (e.g. Structure from Motion algorithms) have been used to create 3D maps from building photographs for an immaterial cost (Snaveley, Seitz, & Szeliski, 2008), but these depend on the availability of photographs, which restricts coverage to only the most significant locations or

requires deliberate data collection.

This paper proposes the use of automated collection of Global Navigation Satellite System (GNSS) data to find GNSS signal patterns and to create 3D maps with level-of-detail 1 (also known as 2.5D). GNSS signal patterns can be used to create 3D maps because the signals can be blocked or affected only when they interact with the environment and obstacles such as buildings. The advantage of GNSS data is that smartphones already collect the required data to facilitate their location-based services. This allows volunteers to passively contribute VGI by sharing their data. The use of passive contributions of GNSS data has been shown to improve the quality of 2D VGI maps beyond active contributions (Basiri, Amirian, & Mooney, 2016). GNSS technology is well-suited to a VGI project as it is a familiar technology often used in such contexts (Huang et al., 2013); globally available and free-to-use (Langley, Teunissen, & Montenbruck, 2017); and easily accessible given the high penetration of GNSS-enabled smartphones (European Global Navigation Satellite Systems Agency, 2020). Furthermore, collecting data is straightforward as smartphones running the Android operating system (currently comprising an 85% market share of new phones sold globally (IDC, 2020)) have allowed access to GNSS raw data since version 7.0 introduced in 2016 (Banville & van Diggelen, 2016).

Section 2 describes how a system would work in practice. A GNSS signal is transmitted from a satellite at a known location (based on the signal's timestamp) to a receiver with an estimated position (either via GNSS or another navigation solution). If the signal is Line-Of-Sight (LOS) or multipath, it may provide evidence that there are no intervening objects, and conversely non-line-of-sight (NLOS) or blocked signals

* Corresponding author.

E-mail addresses: Terence.lines@glasgow.ac.uk (T. Lines), Ana.Basiri@glasgow.ac.uk (A. Basiri).

indicate an interaction with one or more obstacles. These data are processed by a map building algorithm to generate the map, as discussed in Section 4.

Classifying GNSS signals between LOS (or multipath) and NLOS is a difficult problem even with specialised equipment and software, but especially for smartphone receivers (Groves et al., 2013). In this regard this paper proposes a GNSS-based map generating algorithm using the theoretical context of computer vision techniques (Section 3), which help to measure and assure the achievable quality, e.g. accuracy. It is important to investigate if a bias in the signal classifier can affect map accuracy; and also how the uncertainty due to the signal classifier can be reproduced in the produced map. GNSS mapping works published to-date, as described in Section 3, demonstrate different proposed algorithms but have not yet addressed these points. Their results (Irish et al., 2014a, 2014b; Isaacs et al., 2014; Kim et al., 2008; Rodrigues & Aguiar, 2019; Swinford, 2005; Weissman et al., 2013) rely on ad hoc justifications for the chosen parameters or use non-generalisable training datasets of labelled signals, which is addressed in this paper.

We introduce a new mapping algorithm (Section 4) which is designed to be robust to bias in the signal classifier, and to provide principled estimates of the uncertainty in the map output. We apply the algorithm to empirical data collected in a range of urban environments within London and show that it performs consistently across a wide range of initial signal classifiers (Section 5).

This paper is structured as follows: Section 2 describes the properties of GNSS required to understand the remainder of the paper. Section 3 discusses 3D mapping and computer vision-based algorithms. Section 4 proposes the 3D mapping algorithm using GNSS and Section 5 implements the algorithm and tests its performance. Section 6 discusses how the algorithm could be scaled up to a system built upon contribution of data from volunteers at a city-wide scale.

2. Overview of GNSS

At any time, GNSS receivers may receive multiple radio signals transmitted from orbiting navigation satellites. Guides to the principles of a GNSS system are widely available, for example the book “Gnss data processing. volume 1: Fundamentals and algorithms” by Subirana, Zornoza, and Hernández-Pajares (2013). It describes the GNSS signal as comprising a ranging code, also known as the pseudo-random-noise (PRN) code, and navigation data. The receiver uses the ranging code to identify the transmitting satellite and calculate the signal travel time from satellite to receiver, which is multiplied by the speed of light to provide the apparent distance, known as the pseudorange (2013, p. 65). The navigation data provides information on the satellite location along with supplementary information (2013, pp. 18–37). Knowledge of satellite locations and pseudoranges allows the receiver to calculate its position and time if enough satellites (usually 4 or more) are received (2013, pp. 18–37).

The GNSS signals are used in 3 parts of the proposed 3D mapping system. Firstly, the GNSS position solution can be used to estimate the receiver location and timestamp the signals, although this is optional if other location estimates, including map or street view matching from the user inputs, are available. Likewise the receiver’s own clock can be used if the time can not be calculated. Secondly, the timestamp is used to obtain satellite positions from an authoritative reference such as the Navigation Support Office at the European Space Agency (Mayer et al., 2019). Using an external reference, as opposed to transmitted navigation data, provides the location of all satellites including those without received signals. Lastly, the signal can be classified in relation to its propagation path, as detailed below, using signal features such as the pseudorange and the Carrier-to-Noise ratio (C/N_0). The C/N_0 is not directly part of the transmitted information but is a measurement by the receiver of the strength of the received signal.

Like other radio-waves, GNSS signals can propagate to the receiver via a number of different paths. Each path may involve different

interactions with the environment, and each signal can be made up of multiple path components. As illustrated in Fig. 1, this leads to classifying GNSS signals into 4 types:

- if the signal comprises one path without intervening obstacles, it is line-of-sight (LOS) (see Fig. 1, top-left),
- if the signal comprises one path that has been reflected or diffracted (the bending of a signal around an edge) by obstacles, it is known as non-line-of-sight (NLOS) (see Fig. 1, bottom-right),
- if the signal comprises multiple components, which may include a LOS component or be entirely NLOS, it is “multipath” (see Fig. 1, top-right),
- if no signal is received at all it is blocked (see Fig. 1, bottom-left).

For the purpose of 3D mapping, we must distinguish between a LOS component being present (LOS or multipath with a LOS component) or absent (blocked, NLOS or multipath without a LOS component). The identification of NLOS and multipath signals is the basis of many approaches to improving GNSS positioning accuracy in urban locations, however reliably distinguishing between LOS and NLOS signal components is a challenging problem (Breßler et al., 2016). Smartphone receivers are particularly prone to receiving NLOS signals because their linearly-polarised antenna are equally sensitive to LOS and reflected signals, whereas professional or traditional geodetic receivers are less sensitive to reflected signals (Chen et al., 2012). At the same time, there are few techniques to identify NLOS signals using a smartphone, because of hardware limitations relating to cost, size and power consumption (Groves et al., 2013). Three main types of approach have been identified as suitable for smartphones, as detailed below.

The first set of approaches classify signals based on the environment, either using satellite elevation on the principle that a low elevation signals are more likely to be blocked by obstacles (Yozevitch, Moshe, & Weissman, 2016), or using a 3D city model as part of the position solution to jointly estimate position and identify NLOS signals (Bourdeau, Sahmoudi, & Tourneret, 2012; Obst, Bauer, & Wanielik, 2012; Peyraud et al., 2013; Wang, Groves, & Ziebart, 2013; Yozevitch, Ben-Moshe, & Dvir, 2014). This is the inverse problem to creating a 3D map, hence such methods are not directly applicable to 3D map creation.

The second set of approaches identify signals that are likely to be NLOS because the indirect path travelled makes their observed measurements, primarily pseudorange, inconsistent with other measurements. These include calculating position solutions using different combinations of GNSS signals at the same epoch (Groves & Jiang, 2013; Jiang et al., 2011); comparing measurements from other sensors in an integrated positioning system (Soloviev & Van Graas, 2009); and comparing measurements against prior position estimates using Kalman filters (Groves et al., 2013). Jiang et al. (2011) showed that consistency checking has limited sensitivity for a typical (single-frequency) smartphone receiver as errors due to the atmosphere’s effect can be as large as typical pseudorange errors. Furthermore, they depend on the accuracy of other measurements, and in complex urban environments with many reflected signals consistent pseudoranges can be generated by different subsets of NLOS observations (Jiang & Groves, 2012).

The third set of approaches use the carrier-to-noise ratio or derived measures to classify the signal. These approaches are based upon the signal attenuating when interacting with obstacles, however the effects of signal propagation are well-known to be more complex, as described by Molisch (2011). Reflections that cause NLOS signals vary depend on the reflecting surface and the angle of reflection. The signal can be scattered on reflection from a rough surface, leading to a weaker signal in several directions (2011, pp. 64–66), or specular reflection can be generated by a smooth surface, leading to a strong signal in a particular direction (2011, pp. 49–51). Likewise, the effect on signal-strength depends on the degree of diffraction (2011, pp. 54–63). Furthermore multipath signals have a larger variance in their C/N_0 because of small-scale fading, the effect of relative phase on superposition of combining signals (2011, pp. 27–29). As a result, it is possible for a specular reflection to be recorded as strong as or even stronger than a LOS signal

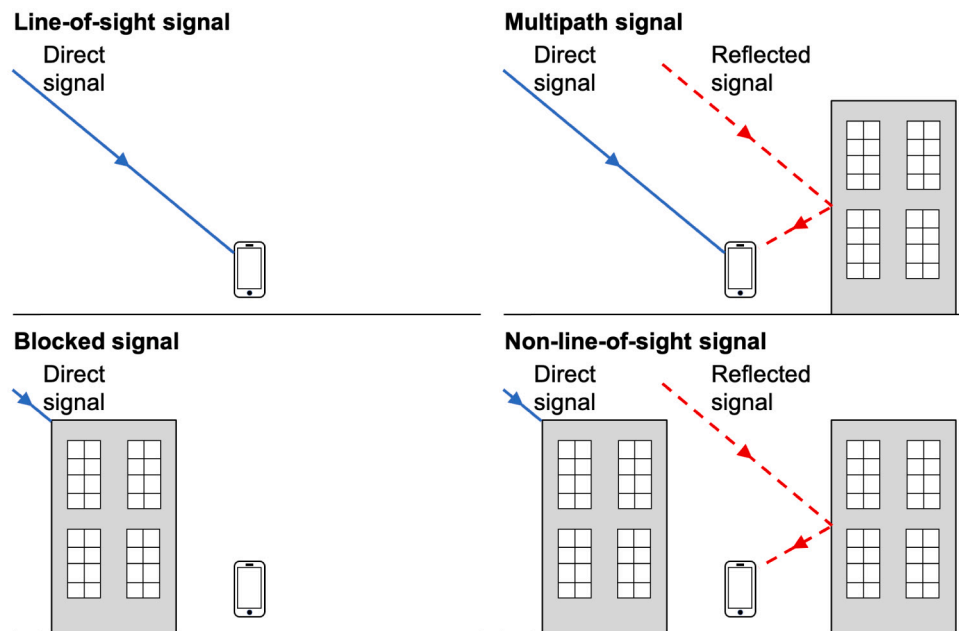


Fig. 1. GNSS signal types.

(Groves et al., 2013), and a GNSS signal can still be received at up to 5 degrees of diffraction (Bradbury, 2007). Because of this, a smartphone GNSS receiver in an urban environment may produce highly overlapping C/N_0 distributions for LOS and NLOS signals (Wang et al., 2015) and C/N_0 can be an inaccurate NLOS classifier (Yozevitch et al., 2016).

As a further source of difficulty, the C/N_0 can also be affected by non-propagation errors: receiver gain varies by smartphone make, model, and orientation (Chen et al., 2012); satellite transmission power varies across constellations and the individual satellites due to different generations of specification and a decrease in power as satellites age (Steigenberger, Thoenert, & Montenbruck, 2018); GNSS signals can be affected by atmospheric conditions (Kintner, Humphreys, & Hinks, 2009) as well as features that are temporary or too small to be included on a map, such as road vehicles or foliage on trees; and the human body attenuates signals, as well as any bag or container in which the smartphone may be placed (Bancroft et al., 2011). Many of these different errors cannot be detected or mitigated in a crowd-sourcing situation due to the range of devices and varying methods of collection (Rodrigues & Aguiar, 2019). Therefore any carrier-to-noise classifier calibrated under training conditions is likely to underperform when tested in real world scenarios.

Applying machine learning methods to creating a NLOS classifier by combining features such as C/N_0 , pseudorange, elevation, and Doppler shift has been investigated using decision trees (Yozevitch et al., 2016), support vector machines (hsu2017gnss, xu2020machine), nearest neighbours and neural networks (Xu et al., 2018). However evidence for an improvement in accuracy against a untrained Naive Bayesian classifier on C/N_0 is mixed: Hsu (2017) showed an increase in accuracy from 67% to 75% and Yozevitch et al. (2016) showed a decrease in false positives from 45% to around 20%, however other works (Xu et al., 2018; Xu et al., 2020) considering multiple situations showed the simpler classifier had similarly or better accuracy in some situations. It has not been shown that any improvements generalise beyond the original experimental settings.

The highly overlapping C/N_0 distributions are suited to a probabilistic classifier. Irish et al. (2014b) used a Bayes classifier based on a Rician distribution for multipath C/N_0 and log-normal distribution for NLOS, which are the canonical forms (Molisch, 2011). A quadratic spline form for the probability density function was proposed by Wang

et al. (2015). This paper proposes a 4-parameter logistic curve (Healy, 1972) for the classifier form. It is a natural choice for a probabilistic classifier as an extension of logistic regression, as discussed in more detail in Section 5. In common with all other approaches mentioned, its performance relies on the fitted parameters and is subject to the same criticisms with respect to performance in a more general setting.

3. 3D mapping as computer vision

Methods for generating 3D models of buildings using existing technologies are surveyed by Wang et al. (2013) and categorised as either image-based (for example photogrammetry) or range-based (for example LIDAR), or perhaps a fusion of the two. While GNSS is a range-based technology for the purposes of navigation, the measured range is of the satellite and not of the environment we wish to map. However by classifying each signal and considering the satellites' relative positions from the receiver, it is possible to derive an image, known as a skyplot, from the original measurements. This shows the set of satellite observations from a receiver at a single epoch, as illustrated in Fig. 2. Similar to a silhouette image, it only shows whether the direct ray to each satellite was open (when the signal is LOS or multipath with a LOS component) or closed (when the signal is blocked, NLOS or multipath without a LOS component). These images can then be used to generate a 3D map through techniques that have similarities to existing image-based techniques.

The earliest image-based approaches relied on knowing the position and calibrating parameters that produced each image, known as the "camera poses" (Cyganek & Paul Siebert, 2009), and primarily used multi-view stereo (MVS) correspondence (Furukawa & Hernández, 2015), where stereographic correspondence determines depth across a collection of overlapping images from multiple viewpoints. More recent approaches use feature identification and matching across images, for example to recover camera pose (Remondino & El-Hakim, 2006), however, a camera image is a complete set of observations across a lens' view, whereas a skyplot is an extremely sparse set of observations, which makes it impossible to identify common features between two images. As common features cannot be identified between GNSS images, a set of MVS techniques apply which use a negative deduction process: assuming the 3D-map has a particular shape, checking how it appears in

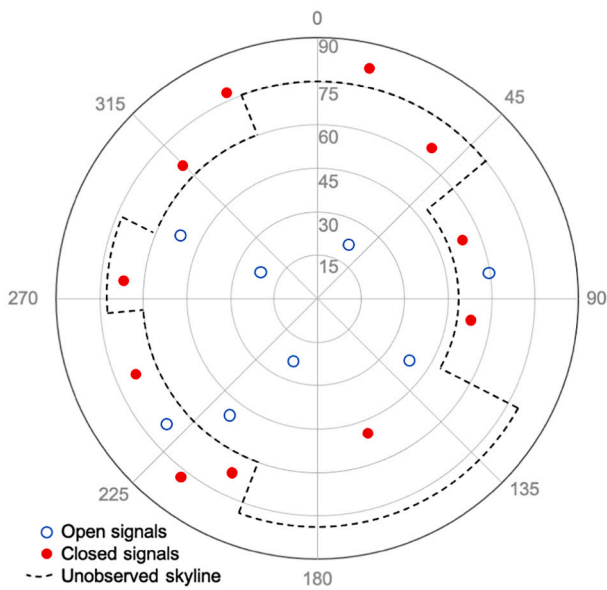


Fig. 2. Typical skyplot (azimuth-elevation graph) with classified signals.

all the images, and iteratively improving the parts of the object which are inconsistent with the images. Such MVS techniques have been shown to produce sub-millimetre accuracy in lab testing (Seitz et al., 2006).

GNSS data does not allow a straight-forward application of existing MVS techniques because it is not possible to measure the consistency of the 3D-map to the skyplots with the same precision. This arises because unlike a picture, where parts of images can be compared by several continuous features such as hue, intensity, and brightness, the skyplot only provides the outcomes of a binary classifier with limited accuracy, which limits how consistency can be measured. The limitations of GNSS classification have been discussed in detail in Section 2. As a second problem, inaccuracy of receiver position may cause the skyplots to be compared to the incorrect part of the 3D-map. The accuracy of the receiver position may vary depending on how the position is estimated: GNSS position fixes are a natural automatic positioning mechanism, but horizontal errors in built-up urban locations may be up to 50 metres for a smartphone (Wang et al., 2015); the receiver estimate could also be provided by the user, leading to a semi-automated process subject to existing questions of volunteered data quality (Fan et al., 2014).

While these problems may limit the detail of the produced 3D-map, GNSS mapping is an alternative to existing 3D-map creation at the scale of a city, which historically utilises airborne methods focused on coarse modelling with geometrically simple building and roof structures

Table 1
GNSS mapping algorithms.

Technique	Scene representation	Photo-consistency	Visibility model	Shape priors	Reconstruction algorithm	Initialisation requirement	LOD
Swinford (2005)	Voxel – 1 metre cubes	N/A. NLOS measurements were ignored	Not used	2.5D mapping (columns of occupied voxels must have no gaps)	Open signals used to progressively remove voxels, as a form of space-carving (Kutulakos & Seitz, 1999)	2D map	1
Kim et al. (2008)	Voxel – unknown size	N/A. LOS measurements ignored	Not used	2.5D mapping	Counts of NLOS measurements used to determine 2D footprint, followed by cost-thresholding of counts to determine height	Bounding box	1
Weissman et al. (2013)	Voxel – unknown size	Hinge-loss function for building height, using height of incorrectly classified signals intersecting a vertical column of voxels	Not used	2.5D mapping	Counts of NLOS measurements used to determine 2D footprint, building height estimated by minimising hinge-loss.	Bounding box	1
Irish et al. (2014a, 2014b)	Voxel – 4 metre cubes	Naive Bayesian probability of a voxel being occupied given set of intersecting signals and a C/N_0 probabilistic classifier	Probability of intervening voxels being unoccupied	None.	Calculates posterior probabilities for each voxel being occupied (modelling as a factor graph and using a sum-product algorithm). Similar technique to probabilistic space carving (Broadhurst, Drummond, & Cipolla, 2001). Extended to allow for gaussian noise in receiver location (Irish et al., 2014a).	Bounding box	N/A - surface extraction unspecified
Isaacs et al. (2014)	Voxel – unknown size	Naive Bayesian probability of a voxel being occupied given set of intersecting signals and a C/N_0 probabilistic classifier	Not used	None.	Calculates probabilities for each voxel through an online learning algorithm that applies the update to all voxels intersected by the signal, by stepping from their current value toward the photo-consistency measure.	Bounding box. Initialised using Irish et al. method	N/A - surface extraction unspecified
Rodrigues and Aguiar (2019)	Voxel – 4 metre cubes	Binary classifier based on C/N_0 features of the set of intersecting signals, with several machine learning methods tried.	Not used	None.	Applies a trained classifier to each voxel, with intersecting signals weighted to allow uncertainty in receiver location	Bounding box	1
4PL-B (proposed in Section 4)	2D surface mesh	The likelihood of a building’s classifier given the observed set of signals (classified by signal features)	Not used	2.5D mapping. All buildings have a single height parameter	On a building-by-building basis: maximum likelihood of the associated four-parameter logistic regression with intersection height as the independent variable	2D map	1

(Lafarge & Mallet, 2012; Zebedin et al., 2006). CityGML, the Open Geospatial Consortium standard for 3D models, defines 5 increasing Levels Of Detail (LOD) with LOD 1 representing each building as an extruded block with flat roof (Kolbe, 2009). LOD 1 is sufficient for many 3D mapping applications (Biljecki et al., 2015; Biljecki et al., 2016) and is often a target for large scale 3D-map production (Dukai, Ledoux, & Stoter, 2019; Girindran et al., 2020).

To understand these limitations in practice, Table 1 categorises existing GNSS-mapping techniques and the algorithm proposed in this paper (Section 4) against a taxonomy of MVS techniques introduced by Seitz et al. (2006). This categorises an MVS algorithm by six fundamental properties: scene representation, photo-consistency measure, visibility model, shape prior, reconstruction algorithm, and initialisation requirements. As an additional category, we add the LOD of the produced map.

1. Scene representation is how the object geometry is represented. Primary types are voxel (a 3D grid of pixels) or a 2D surface mesh. Many reconstruction algorithms require a particular representation.
2. Photo-consistency is a measure of the consistency between images to determine whether an object reconstruction (which defines the projected images) is consistent with a set of images.
3. Visibility model is the method by which images are selected when evaluating photo-consistency measures. It is important to exclude images where the object is occluded.
4. Shape priors guide the reconstruction algorithm to produce desired object characteristics such as smoothness and maximal or minimal surface area or volume.
5. Reconstruction algorithm is the method of producing the reconstruction. Non-feature based methods typically work by minimising inconsistency cost either i) point-by-point (cost function defined for each scene position and surface extracted based on a cost threshold); or ii) globally (cost function defined for an object surface)
6. The initialisation requirement provides constraints on scene geometry. Many algorithms require constraints (for example a bounding box) to function, and may obtain different solutions depending on their initialisation.

Existing GNSS mapping algorithms seem to be relatively simplistic compared to existing MVS algorithms. They are primarily distinguished by their varying approaches to photo-consistency, which reflects the limitations discussed above. However, none of the approaches to date are satisfactory for generating even an LOD 1 map. This is because the measurements of photo-consistency either ignore inconsistent classifications (Kim et al., 2008; Swinford, 2005), or rely on a pre-specified signal strength classifier to turn signal strength observations into a cost (Irish et al., 2014a, 2014b; Isaacs et al., 2014; Rodrigues & Aguiar, 2019; Weissman et al., 2013), taking for granted that the classifier model is unbiased. The probabilistic approaches of Irish et al. (2014b) and Isaacs et al. (2014) are potentially more robust because they effectively give a higher weighting to observations with a more certain classification, however the effect of model misspecification has not been investigated.

The algorithms also do not specify how uncertainty in the photo-consistency measure (due to signal classification error and location error) should be reflected in the reconstruction algorithm. We emphasise that the probabilistic approaches do not address this, as all posterior probabilities will converge to 0 or 1 with a large enough data set. The probabilistic approaches do not specify how a surface should be extracted from the voxel probabilities, but probabilistic space carving is typically used with a cost-minimisation approach, where cost would include negative likelihood as well as potential shape priors. It is possible to reflect uncertainty through considering the sensitivity of cost to changes in the map, however cost sensitivity is also a function of the chosen classifier and size of the data set, making such approaches problematic. The algorithm we introduce in the next section seeks to

address both problems of bias and uncertainty.

4. GNSS-mapping algorithm

Our proposed GNSS mapping technique directly generates a 3D map by using it as a signal classifier and solving the inversion problem given the observed signal data, similar to the MVS approach known as statistical inverse ray tracing (Liu & Cooper, 2011). The technique is applied to a single building at a time, using an existing 2D map to provide a building footprint. The set of GNSS observations that intersect the 2D footprint form a dataset of (intersection height, signal features) pairs, as illustrated in Fig. 3. The 3D map is extruded from the 2D footprint with the building height as an unknown parameter. The technique uses a classifier based on signal features to label the GNSS signals and the labelled signals are used as data to estimate the building height, as detailed below. This process is then reversed with signals labelled as open or closed depending on whether they intersect the 3D building, and these relabelled signals are used to train the signal classifier. This process iterates to improve the building height estimates. Table 1 categorises the algorithm alongside existing approaches.

The proposed algorithm has three novel aspects relating to the photo-consistency problem:

- Firstly, it considers intersection height as a probabilistic classifier, using a four-parameter logistic regression (4PL) as defined below as the classifier form for each building. This leads to a natural interpretation of height uncertainty from the certainty of the classifier.
- Secondly, rather than generating the map by maximising its accuracy as a classifier, which creates unwanted dependence on the bias of the signal feature classifier, it relates the map classifier parameters to the physical map, based on our understanding of the typical measurement errors of the observations.
- Thirdly, once an initial map is generated, it is used to reclassify the signals and refit the signal feature classifier, before repeating in a bootstrapping approach. This takes advantage of shape priors to improve the map beyond observed data.

These aspects are discussed further following the details of the technique, which is set out as the following pseudo-code 1. For simplicity it assumes the only signal feature used for classification is the carrier-to-noise ratio, however any signal classifier could be used, as long as it is class-conditionally independent of height, and Section 2 contains more detail on potential classifiers.

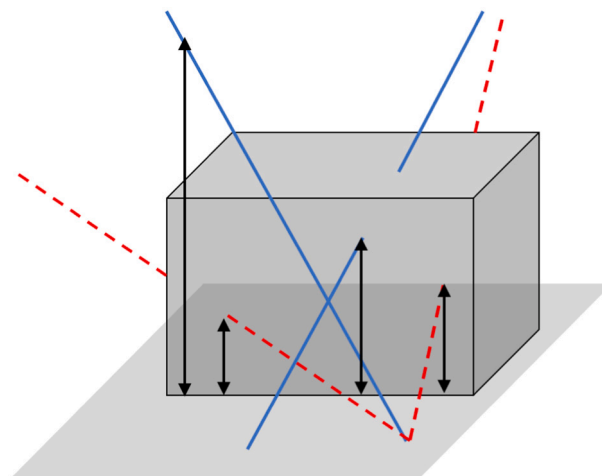


Fig. 3. Example of building data generated for 2.5D mapping from footprint intersection heights and signal classifications.

Algorithm 1: 4PL-B algorithm

```

function SignalClassifier (param,ss):
    /* signal strength classifier, with heuristic initial parameters */
    if ss=n/a then return 0 else return Pr(ss);

function 4PL ((a,b,c,d),h):
    /* four parameter logistic regression associated with the building, with
       intersection height as the independent feature used to classify signals */
    return Pr(h);

input : A set X of observation tuples (y,ss,h) for a building
        y: signal label (initially blank)
        ss:  $C/N_0$  (n/a if blocked)
        h: intersection height

output: Parameters (a, b, c, d) of 4PL
         $c + 1.5/b$ : height point estimate
         $(c, c + 3/b)$ : height range estimate

repeat
    for (y,ss,h) ∈ X do  $y \leftarrow \begin{cases} 1 & \text{SignalClassifier}(\text{param}, \text{ss}) > 0.5 \\ 0 & \text{o'wise} \end{cases}$ ;
    (a, b, c, d) ← maximum likelihood estimates for 4PL given X
    for (y,ss,h) ∈ X do  $y \leftarrow \begin{cases} 1 & h > c \\ 0 & \text{o'wise} \end{cases}$ ;
    param ← maximum likelihood estimates for SignalClassifier given X
until (a, b, c, d) have converged;

```

A 4PL extends logistic regression to consider asymptotic probabilities other than 0 or 1 (Healy, 1972). It has the following univariate form:

$$Pr(x) = d + \frac{a - d}{1 + \exp(-b(x - c))}$$

where a and d are the upper and lower asymptotes, respectively, and b and c are the standard linear coefficients in x . The 3D mapping algorithm uses the maximum likelihood estimates of the 4PL parameters, which can usually be obtained through standard optimisation methods although the EM algorithm has been proposed as a superior alternative (Dinse, 2011). Gradient descent methods (Ruder, 2016) can also be used to optimise the parameters, which raises the possibility of using stochastic gradient descent on the classifiers and performing batch-updates on each classifier in turn, in order to allow the 3D map to be updated over time as new data is collected.

The use of the 4PL is integral to the proposed technique as the parameters have a physical interpretation relating to the observation errors, as illustrated in Fig. 4. Without these errors, an idealised height classifier would be a step function, with zero probability of open signals for intersections below building height and probability of one above building height.

The 4PL asymptotes reflect signal classification error, where a is the positive predictive value, or precision, of the signal classifier and d is the false omission rate (equal to 1 minus the negative predictive value). It is important to clarify that these are primarily the error rates of the signal classifier which has noisily labelled the data, and not the error rates for the map classifier against the true unknown labels.

The scaling parameter b relates to the uncertainties in building height, for reasons including unmodelled effects such as diffraction effects and the complexities of building roofline, and measurement errors such as incorrect intersection height due to receiver location errors. A gentle slope indicates a lower level of certainty in building height as the effect of height on signal class is prolonged, whereas a steep slope indicates more certainty due to an abrupt height effect.

The inflection point c , relates to the unknown building height. The b and c parameters generate a height estimate of $c + 1.5/b$ with a range between $(c, c + 3/b)$ as explained below.

The rationale for this approach is that the GNSS received signal strength and intersection height can be treated as class-conditionally independent, with the exception of diffraction effects and height errors. Class-conditionally independent means that within a signal classification (open or closed) the signal strength is independent of the intersection height: for open signals (where the signal intersection

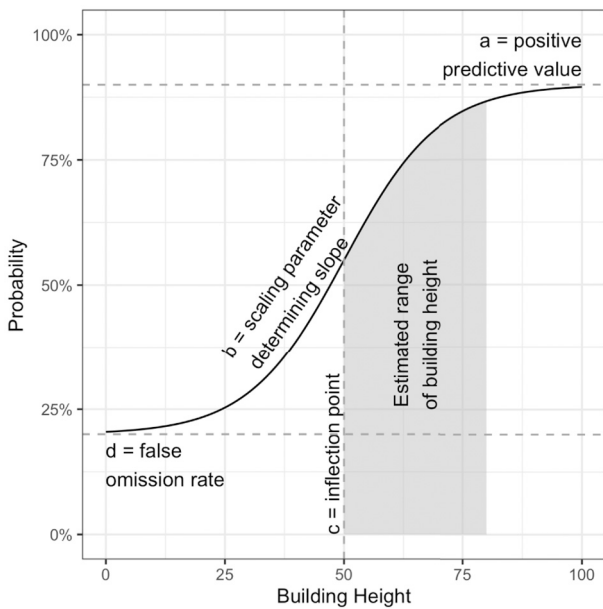


Fig. 4. Four-parameter logistic regression.

height is above the building height) there is a LOS component which does not interact with any obstacles and this is unaffected by intersection height; likewise, for closed signals (where the signal intersection height is below the building height), the LOS component has been blocked and this is unaffected by the intersection height.

This is a generalisation: the contribution of multipath and NLOS components as well as any effects of unmapped objects on LOS components will depend on position but with a reasonable spatial

distribution of observations around the building the dependence on height is presumed to be ignorable; the algorithm also assumes that the blockage of signals by other buildings (which will have a height dependence) does not have an effect, but this is a similar approach to other MVS algorithms, which correct for this problem using a visibility model rather than in the photo-consistency measure; the remaining dependence comes from diffraction effects and height errors, which are explicitly accounted for in the algorithm.

When diffraction effects and height errors are negligible, the class probability (which is measuring the consistency of the signal strength classifier and map classifier) is independent of intersection height, as represented by the asymptotes of the 4PL with zero gradient. As the intersection height approaches the building height from either direction, a growing proportion of signals may be misclassified by the map due to height errors. This occurs when the intersection height is between the modelled building height (which is modelled as uniform across the building) and the actual building height, which varies across the building with roofline complexity, or conversely, when the actual building height is between the measured and actual intersection height due to receiver location errors.

These effects lead to a slope between the asymptotes instead of a step, however the effect of intersection height errors should be symmetric, and therefore not affect c , the inflection point of the 4PL. The effect of non-uniform building height will shift c to the average building height across the observations, which should be a good approximation of the true average building height with spatial diversity of observations.

On the other hand, diffraction effects depend on the degree of diffraction of the signal which depends on both the distance of the receiver as well as the difference between building height and intersection height. As a simplification, the algorithm assumes that the height difference is a proxy for the degree of diffraction, and as this decreases the signal attenuation lessens, leading to an increasing number of LOS classifications.

This is an asymmetric effect, as it only has an effect when the



Fig. 5. Experiment locations above, and photos below. From left to right: UCL, Goodchild Road, Hermitage Road. The outlined polygon is the building footprint according to OS Mastermap, this was used in the algorithm with the background map tile for illustration only. Background map tile: Google, ©2021 Bluesky, CNES/Airbus, Getmapping plc, Infoterra Ltd. & Bluesky, Maxar Technologies, The GeoInformation Group.

intersection height is below the building height. This has the effect of shifting the inflection point c below the true building height, therefore the building height should be above the inflection point and toward the upper asymptote. Given the uncertainty of the relative magnitude of intersection height error and diffraction effect, we conservatively suggest a point estimate of $c + 1.5/b$ and range between $(c, c + 3/b)$, which represents the 50% to 95% percentile of the distance between the asymptotes.

It follows from this formulation that our estimate does not impose any additional assumptions on the signal strength classification accuracy, whereas a solution provided by a cost-minimisation approach depends on the signal classification model being an unbiased classifier. The proposed approach provides a height estimate that is robust to model bias and also provides a measure of uncertainty in the height due to the underlying measurement uncertainty.

In order to improve the classification accuracy, this paper builds upon the class-conditionally independency of GNSS signal strength and height, and uses a co-training approach to label data more confidently through an iterative process. Blum and Mitchell (1998) introduced co-training as a form of disagreement-based semi-supervised learning, which uses a pair of binary classifiers to label a dataset by iteratively applying each classifier and using the most confidently labelled instances as training data for the other classifier. In the straightforward bootstrapping approach we take here, we consider all labelled signals as training data, and stop when the map classifier parameters converge. This does not require the two classifiers to have consistent labels, but indicates that the classifiers are class-conditionally independent.

5. Implementation

To verify the accuracy of our proposed algorithm, we estimated the height of a range of buildings in different urban environments in greater London by collecting GNSS observations nearby and using them as inputs into the proposed algorithm. The next subsections describe the experimental setup and algorithm results.

5.1. Experiment

Urban environments in greater London vary in use, street width, building height and density, and construction material. To compare algorithm performance in different environments, three representative buildings are presented which cover a wide range of building heights, construction materials, and sky visibility (see Fig. 5). The first is the main estate of University College London, the second is a block of flats (Goodchild Road) in an urban canyon, and the third is a terrace of houses (Hermitage Road) in a residential setting. The university estate is a building of significant height and mass, built primarily from stone in the 19th century, with nearby open space allowing spatial diversity of data collection. The block of flats represents modern inner-city construction: it is of moderate height in a high-density location, built within the last 20 years from reinforced concrete with a brick and glass facade, the observations were made from a narrow pedestrianised street with visibility to the sky only at high elevations. The terrace is low density and low height, it is brick-construction from early 20th century, and the

Table 2
Summary of collected data.

Site ID	Recorded				
Number of signals observed	Epochs	Recorded	Blocked	Total	Intersecting
UCL	3558	88,633	5284	93,917	88,106
Goodchild Rd	8136	227,658	21,718	249,376	95,362
Hermitage Rd	8350	26,094	310,618	336,712	100,884

observations were made with a restricted collection protocol from the far side of the street to maximise the number of received low elevation signals.

A Samsung Galaxy 10 running the Android 10.0 operating system was used as the GNSS receiver. It supports the four major GNSS constellations: Global Positioning System (GPS), GLObal NAVigation Satellite System (GLONASS), Beidou, and Galileo. Multi-constellation receivers such as these ones are now standard and embedded in many mobile devices (ESA, 2020), and result in a device typically having potential LOS to 30 to 50 GNSS satellites above the horizon at all times. As described further in Section 6, Android phones allow access to “raw” GNSS data for all signals, along with associated GNSS receiver position solutions. We developed a recording app based on Google’s GNSS Logger (Banville & van Diggelen, 2016) that accesses the raw data for the position solution and satellite identifier, used to determine the direct signal path, and the carrier-to-noise density, used to classify the signal. The app also allows manual recording of observer locations.

For each site the receiver was placed in a static location and measurements were recorded as a stream of data measured at 1 Hz frequency for a duration of around 30 minutes. This was undertaken twice at UCL, and 5 and 6 times at the Hermitage Road and Goodchild Road sites respectively, at different locations and times of day to allow the satellite geometries to change. The varying frequency of measurements across sites were to provide similar numbers of intersecting signals across the different sizes and shapes of floorplates. The dataset is summarised in Table 2. The observer locations were manually inputted based on a visual determination against a small-scale map, with an estimated location error of below 2 metres. Results are presented in this paper for both the more accurate manually input locations and the automatic GNSS position solutions.

For each observation time, all satellite positions were retrieved using information on satellite orbits freely available from the Navigation Support Office at the European Space Agency, which allowed the dataset to be expanded to blocked signals for all receiver-supported constellations. An elevation filter was applied to remove low elevation signals, as these are often blocked by background and unmapped objects. The elevation filter was set at 10 degrees for the UCL and Goodchild Road sites, and 0 degrees for the Hermitage Road site, where the recordings were made from a relative distance and position such that many low elevation signals were received. As a last step, observations with a satellite elevation above 85 degrees were also removed, because at these elevations trigonometry implies errors in the observer’s horizontal position are magnified 11 times or more in calculations of intersection height, making the data unacceptably poor quality. The elevation was calculated with respect to the tangential plane on the WGS84 ellipsoid.

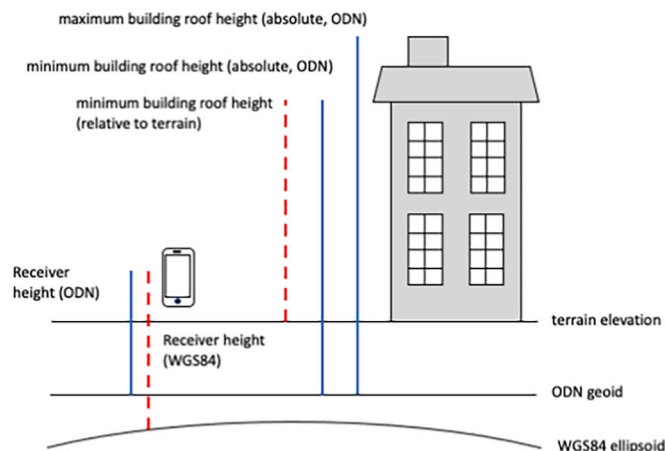


Fig. 6. Building height definitions.

Table 3
Building heights.

Site	UCL	Goodchild Road	Hermitage Road
OS Height (min-max)	43.8 m - 47.1 m	–	–
Google Earth (min-max)	44.0 m - 47.0 m	47.0 m	33.0–35.0 m
Representative LOD1 height	46.0 m	47.0 m	34.0 m
Indicative ground elevation	26.0 m	31.0 m	24.0 m
Indicative relative building height	20.0 m	16.0 m	10.0 m

The building footprints were obtained from the Ordnance Survey GB, Great Britain’s national mapping agency. Ordnance Survey’s MasterMap (Ordnance Survey, 2020c), provides the benchmark map for the country, in terms of reliability and accuracy. GNSS elevation data is collected by a receiver with reference to the WGS84 ellipsoid. It was converted using accurate transformation grids, as described in Ordnance Survey (2020a), to the coordinate reference system used by OS Mastermap: British National Grid for horizontal coordinates and Ordnance Datum Nelwyn (ODN), a local geoid, for heights. Fig. 6 illustrates the conversion between ODN and WGS84 and the relation between absolute building height and relative building height from terrain. The results in this paper are reported as absolute heights with reference to ODN. It also illustrates how building heights in a LOD 1 model depend on the choice of geometric reference: the lowest or highest point of a roof may be used, or any ad-hoc point or average of points in-between (Biljecki et al., 2016).

The building heights, shown in Table 3, were obtained from OS MasterMap (Ordnance Survey, 2020b) where available, and Google Earth (Google, 2020), and represent the minimum and maximum heights across the buildings, with the UCL building being particularly complex with a large dome and varying levels. For the UCL building, the adopted height in the paper is the height of the Library entrance hall, which we believe is representative of the larger building. While this is a subjective choice, the value of our algorithm lies in its consistent results over a range of starting conditions, and this conclusion holds for any reasonable adopted height for the UCL building. We adopt the midpoint of the height range as the ground truth height. Table 3 also shows the indicative ground elevation and relative building heights, determined

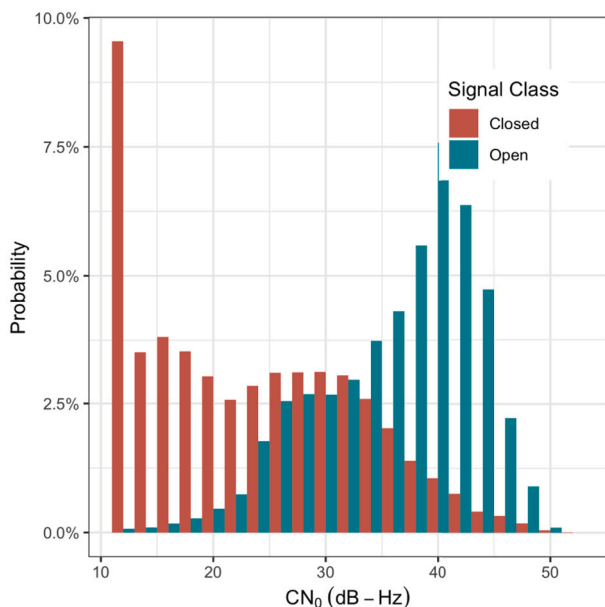


Fig. 7. Distribution of received signals.

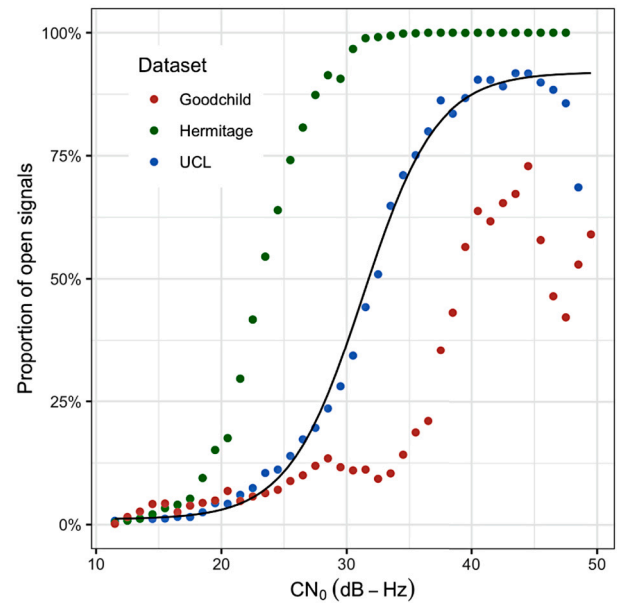


Fig. 8. Distribution of received signals.

using the OS Terrain 5 Digital Elevation Model (Ordnance Survey, 2020d).

To calculate the intersection height at which the LOS component of each signal would intersect the building, it was assumed that the signal travelled in a direct line with respect to the projected plane coordinate system. This neglects earth curvature, however for all plausible observations with at most 1 km distance between an observer and a building, the effect is only 8 cm. Likewise curvature of the signal due to atmospheric diffraction is less than 0.8 arcseconds, which equates to less than 1 cm effect at 1 km (Möller & Landskron, 2019).

5.2. Results

5.2.1. Signal classifier

GNSS mapping algorithms rely on a signal classifier to predict whether a signal was open (LOS or multipath with a LOS component) or closed (blocked, NLOS or multipath without a LOS component), and the performance of the signal classifier plays an important role in the quality of the produced map. It is important to investigate if bias and uncertainty in the signal classifier affects the produced map.

This paper classifies individual signals by their C/N_0 through implementing a 4PL probabilistic classifier, with the most likely classification being assigned. The form of classifier was chosen based on the results of Wang et al. (2015). They proposed a quadratic spline form however we suggest that a 4PL has advantages of monotonicity and smoothness that make model fitting through optimisation more robust. It is worth reminding readers that this has no connection to the 4PL used in the map classifier, but happens to have a form that is a good fit to the observed data. More complex alternative classifiers are discussed in Section 2, and use additional features available as raw data. Likewise, the C/N_0 classifier could be extended to model ionospheric and

Table 4

Test data cross-tabulation by predicted (C/N_0) and actual (Height) class. Height n/a indicates the signal did not intersect the building.

		Height Class			Total
		Open	Closed	n/a	
C/N_0 Class	Open	40,683	27,474	95,062	163,219
	Closed	23,750	104,339	294,780	422,869
	Total	64,433	131,813	389,842	586,088

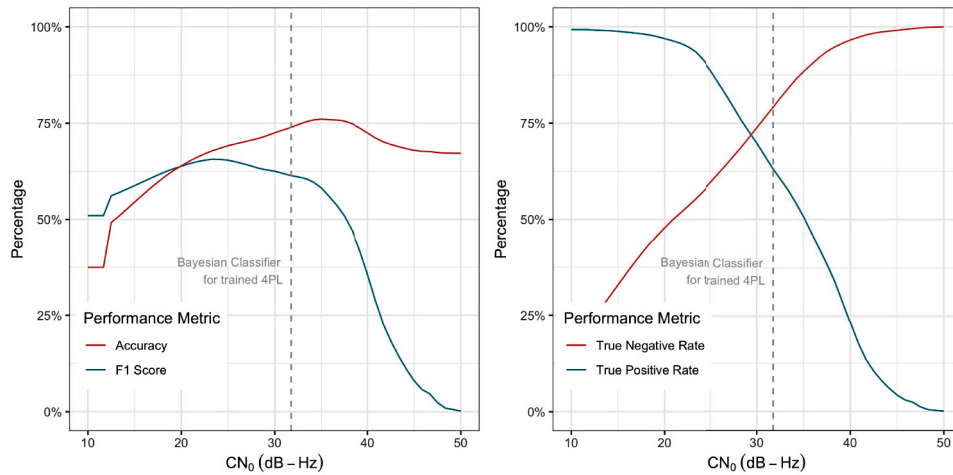


Fig. 9. Signal classifier performance with varying classification thresholds. Highlighted classification value represents the 50% probability class threshold estimated by the trained 4PL.

tropospheric effects as well as taking into account specific device receiver gain and satellite transmission power. These complexities were not implemented in the paper, as the advantage of the proposed algorithm is that the generated map is relatively robust to the accuracy of the classifier.

To assess the performance of the signal strength classifier, the ground truth building heights were used to label the dataset. The C/N_0 distribution of open and closed signals is shown in Fig. 7. The two signal classes have distinct but overlapping distributions, demonstrating the

difficulty of accurately predicting class. Predicting closed signals at low signal strengths can be more straightforward than open signals at high signal strengths, based on the overlap of the two distributions. Almost no signals were received with a C/N_0 of less than 10 dB-Hz, which was an expected effect marking the cutoff below which the signal is too weak to be registered by the receiver. There is an anomalous peak of observations just above this level, which we are unable to explain with any certainty.

A probabilistic 4PL classifier was trained on the dataset pertaining to

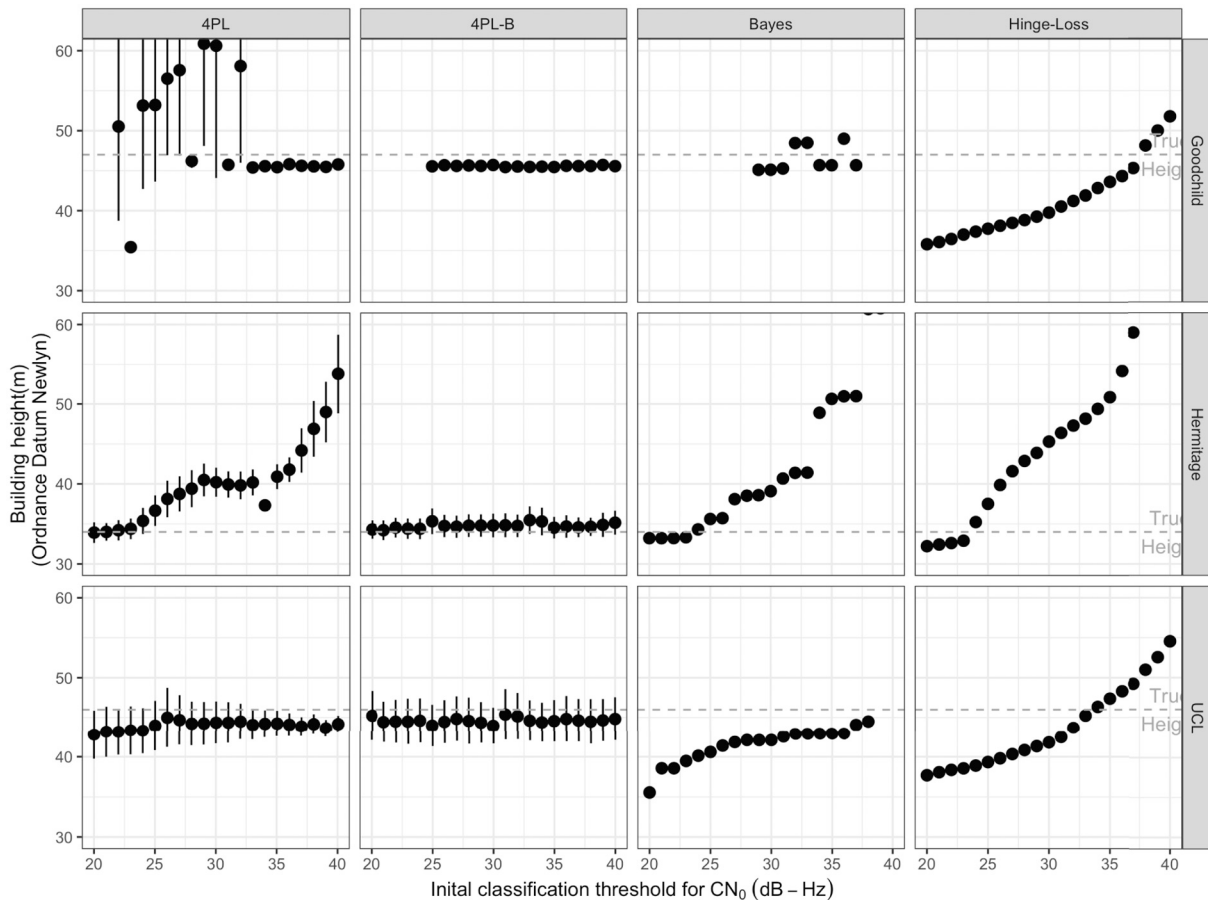


Fig. 10. Mapping algorithm results with varying signal strength classifiers.

Table 5
Root Mean Square Error of mapping algorithms.

	UCL	Goodchild Road	Hermitage Road
Manually input locations			
4PL-B	1.4 m	1.4 m	0.8 m
4PL	2.1 m	11.7 m	7.8 m
Hinge-Loss	5.6 m	7.4 m	20.6 m
Bayes	8.6 m	24.9 m	18.7 m
GNSS position solutions			
4PL-B	0.6 m	–	0.8 m
4PL	1.4 m	28.7 m	19.5 m
Hinge-Loss	5.6 m	10.1 m	9.9 m
Bayes	7.6 m	29.9 m	31.6 m

Calculated for each site across all twenty initialisations. 4PL-B results were excluded where the algorithm did not converge: 5 results for the Goodchild Road site using manual locations; all results at Goodchild Road using GNSS locations; and 4 at the Hermitage Road site using GNSS locations.

the UCL building, and tested on the data from the other locations. Fig. 8 illustrate how the varying observational settings affect the relationship between LOS probability and signal strength. Which decrease the performance of trained signal classifiers. This leads to a stark divergence in performance of the signal strength classifier between training and test data.

The 4PL signal classifier fits the observed proportions for the training data relatively well, with a Mcfadden’s R^2 of 70.7%, but is wrongly parameterised for the test data, with a Mcfadden’s R^2 of 18.9%. The performance of the 4PL across the dataset is shown in Table 4, which cross-tabulates the true labels against the predictions obtained by the trained 4PL, using a 50% probability threshold to label classes. Fig. 9 illustrates the effect on accuracy of changing the classification threshold. The performance of a single classifier across the combined test locations can only be improved marginally by optimising parameters. As discussed in Section 2, these parameters are device and location specific, making it difficult to generalise the classifiers.

5.2.2. Map algorithm

To assess the map algorithm, it was applied to each location’s dataset. To evaluate the impact of a misspecified signal classifier, it was repeated using a range of parameters for the initial signal strength classifier. For comparison, the same signal classifier was used in the non-bootstrapped 4PL algorithm, the Weissman et al. (2013) hinge-loss method, and a Bayesian probabilistic method of maximising likelihood similar to Irish et al. (2014a), albeit applied to the entire dataset rather than to each voxel. The signal strength 4PL was initialised with the same initial parameters (a : 0.9, b : 0.2, d : 0.1) except for the inflection point, c , which ranged from 20–40 dB-Hz in 1 db-Hz increments. This generated a range of 50% probability classification thresholds from 20 to 40 dB-Hz, which we believe is a plausible range: the thresholds for our datasets were between 23 and 40 dB-Hz respectively, and other works have

Table 6
Uncertainty reported by 4PL-B algorithm.

	UCL	Goodchild Road	Hermitage Road
Manually input locations			
min-max heights	41.9 m - 47.4 m	45.4 m - 45.8 m	33.4 m - 36.2 m
uncertainty range	5.5 m	0.4 m	2.8 m
GNSS position solutions			
min-max heights	41.5 m - 49.5 m	–	30.7 m - 38.8 m
uncertainty range	8.0 m	–	8.1 m
Google Earth			
min-max heights	44.0 m - 47.0 m	47.0 m	33.0-35.0 m
uncertainty range	3.0 m	0.0 m	2.0 m

Google Earth uncertainty for UCL height is that of the Library entrance hall. The entire building has a height which ranges between 26.0 m–58.0 m (Ordnance Survey, 2020c).

ranged from 23 dB-Hz (Wang et al., 2015) to 37.5 dB-Hz (Yozevitch et al., 2016). The bootstrapping algorithm was stopped at the lower of 10 iterations and fewer than 1% of the labels having changed between two iterations of the map classifier.

Fig. 10 shows the algorithms results when applied to the datasets with the manually inputted, more accurate, receiver locations. The 4PL-B algorithm converged to a solution at all 20 starting conditions at the UCL and Hermitage Road sites, and 15 out of 20 at the Goodchild Road sites. The other non-iterative algorithms always generated a solution (not always shown in the figure due to being outside the limits of the y-axis) however is not necessarily advantageous to return a low quality estimate. Table 5 show the root mean square error for each algorithm and site across all 20 different initialisations. The 4PL-B algorithm is more accurate by an order of magnitude due to its consistency.

Unlike the 4PL-B algorithm, which provides consistent results regardless of initialisation, results for the other methods depend on choice of initialisation. The Weissman hinge-loss algorithm increases superlinearly with initial classification threshold and nothing can be usefully inferred without a knowledge of the optimal classification threshold for the dataset. The Bayesian algorithm results increase monotonically, not smoothly but with stepped increases and relatively stable clustering around certain values. It requires less precise knowledge of the optimal classification threshold but the initial classification must still be relatively accurate otherwise the algorithm can generate wildly inaccurate results. The non-bootstrapped 4PL algorithm performance varies by location. In less challenging locations (UCL) it performs consistently, but in more challenging locations it requires a relatively accurate starting point, similar to the Bayesian approach.

The difficulty that the non-bootstrapped 4PL algorithm has in certain locations appears to be due to the overall balance of collected data. In the two more challenging locations, the environment and data collection protocol was such that most of the data was blocked (Goodchild Road) or open (Hermitage Road). The model is fit to the data as a maximum likelihood estimate with the simplifying assumption that signal strength is independent of height within a class. However there will always be weak patterns of height dependency and signal strength, and if most of the data is within the same class then the model fits weak patterns within the class, due to the weight of data, rather than the stronger pattern across classes which is only present in a small quantity of data. Preliminary work suggests that improvements can be obtained by filtering and rebalancing the data based on the distribution of intersection heights. Improvements to the 4PL algorithm could help broaden the conditions of convergence for the bootstrapped algorithm.

Table 6 shows the 4PL-B algorithm measure of uncertainty around the building height based on the steepness of the 4PL curve, compared to the true height. The algorithm uncertainty is in accordance with the relative complexity of the building shape: Goodchild Road is a simple flat roof, Hermitage Road is a terrace with pitched roofs, and UCL has a complex roof shape.

The process was repeated on the data using the GNSS-provided latitude and longitudes rather than the manually input locations. This increases location errors but fully automates data-collection. We re-ran results using the GNSS-provided latitude and longitudes, and setting the altitude for all signals as 1 m above ground level for the experimental location, using the OS Terrain 5 Digital Elevation Model (Ordnance Survey, 2020d). By using digital elevation models, it is possible to avoid typically large vertical errors in GNSS positioning, which can create intersection height errors. The results are shown in Fig. 11 and Table 5. The 4PL-B algorithm perform relatively accurately at the Hermitage and UCL sites, where satellites were visible at low and moderate elevations but failed completely for the Goodchild site, where only high elevation signals were visible. This is understandable because when only high elevation signals are visible, the GNSS position errors are typically larger due to geometric dilution of precision, and this is compounded because the high elevation also increases the effect of horizontal error on calculated intersection height. The other algorithms showed the same

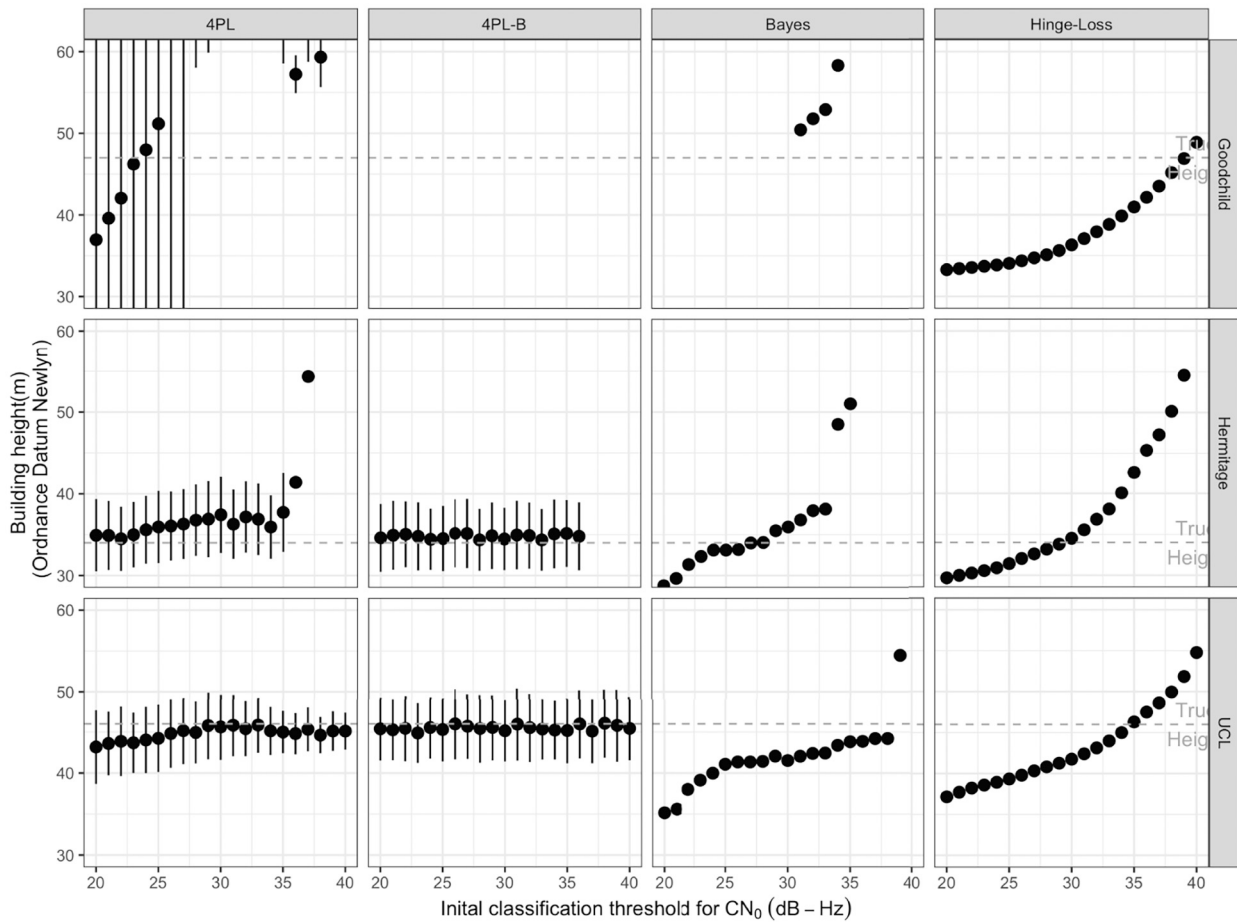


Fig. 11. Mapping algorithm results with GNSS position solutions.

effects. The uncertainty reported by the 4PL-B increased with the GNSS solutions (Table 6) highlighting that the algorithm is able to reflect the quality of the position data in its reported results.

6. Discussion

This section considers how the GNSS mapping algorithm could be scaled up to a VGI system on a city-wide scale. It discusses how a system could be implemented; how the algorithm could be extended to consider occlusion; whether the approach extends to a higher LOD; and the role of location errors.

The key advantage of a GNSS mapping approach is that participation in the VGI project is straightforward and almost entirely passive. The necessary data is already continually collected by GNSS-enabled smartphones to facilitate positioning and the use of location-based services. Since version 7.0 introduced in 2016, the Android operating system allows access to “raw” GNSS data through the android.location Application Programming Interface (API) (European Global Navigation Satellite Systems Agency, 2017), i.e. any installed mobile applications (app) with user permissions can use the GNSS raw data. The API usually provides signal observations at a 1 Hz frequency, and consequently a single smartphone can generate above 100,000 signal observations an hour, including signals that were expected to be received but in practice were blocked due to obstacles between the satellites and the receivers such as buildings.

To implement a large-scale VGI system primarily requires the creation of Android mobile app, which is installed by a participant, and for it to run as needed in the background, with the option of the user manually inputting locations. The app can then periodically upload data to a

central server for processing. GNSS data provided through the API includes all the information required by the various signal classifiers described in Section 2: the GNSS navigation message, from which the satellite and its azimuth and elevation can be identified, along with typical GNSS observables such as pseudorange, carrier phase, precise timing and doppler shift. The carrier-to-noise ratio is also available. Further study is planned to develop a VGI mobile application and address pertinent questions e.g. privacy, incentivisation and participation.

The presented algorithm considers signals being blocked by a single building. On a larger scale, additional occlusion may occur. This could be due to a taller building further away from the receiver in the same direction, or unmapped objects (e.g. buildings due to an outdated base-map; or trees and other street furniture) between the receiver and the building of interest. This would present itself as greater uncertainty and error in the height estimate due to the occlusion effects.

Spatiotemporal diversity of data collection should mitigate many of these errors, as the occlusion will vary based on the receiver position and signal azimuth and elevation. This suggests a more granular extension of the algorithm which groups signals by their direct path. This would lend itself to a higher LOD map, as the estimated height can vary across the building, and also a visibility model where the height estimates from different groups of signals can be compared, and outliers would suggest an occlusion which can then be taken into account by amending the basemap or applying the algorithm to a filtered dataset.

The algorithm itself as a photo-consistency measure can be improved: the four-parameter logistic is fit to the data as a maximum likelihood estimate. If most of the data is within the same class (either because the building is tall and close-by, or small and measured from a

distance) then the model can fit weak patterns within the class, due to the weight of data, rather than the stronger pattern of interest which is only present in a small quantity of data. An extension of the algorithm could attempt to reweight the data as the height estimate develops.

Location error is an important component of the algorithm performance. In urban canyons (narrow streets with tall buildings on either side) it can be expected that the algorithm performance degrades. This is because LOS to GNSS satellites is only possible at a high elevation. This leads to poor cross-street position accuracy (Groves et al., 2012) and the effect of horizontal error on calculated intersection height is magnified. Further study is planned to extend the current algorithm to improve its accuracy in this context: modelling location error and signal diffraction, and using a more complex signal classifier.

7. Conclusion

This paper proposed a novel algorithm that automatically generates 3D LOD 1 maps by processing GNSS data. The technique works on unlabelled signal observations by co-training a signal classifier and having a robust design to any potential bias in the signal classifier. The implementation of the algorithm shows that it is unaffected by bias in the initial data labelling and the results are comparable to existing benchmarks for 3D maps (Open Geospatial Consortium, 2012), although larger scale data collection is required to provide further experimental verification. By providing a low-cost alternative, this work could be very helpful for the large scale production of 3D maps, particularly for regions where the cost of existing technologies is prohibitive. These maps have many useful applications in location-based services, autonomous vehicle and drone navigation, and urban planning.

Declaration of competing interest

The work presented in this paper has been partially funded by the UK Research and Innovation (UKRI) Future Leaders Fellowship MR/S01795X/2.

The authors stated no conflict of interest.

Acknowledgements

The work presented in this paper has been funded by the UK Research and Innovation (UKRI) Future Leaders Fellowship MR/S01795X/2.

References

- Baltsavias, E. P. (1999). Airborne laser scanning: Existing systems and firms and other resources. *ISPRS Journal of Photogrammetry and Remote Sensing*, 54(2), 164–198. [https://doi.org/10.1016/S0924-2716\(99\)00016-7](https://doi.org/10.1016/S0924-2716(99)00016-7).
- Bancroft, J. B., et al. (2011). GNSS antenna-human body interaction. In *Proceedings of the 24th international technical meeting of the satellite division of the institute of navigation (ION GNSS 2011)* (pp. 3952–3958).
- Banville, S., & van Diggelen, F. (2016). Precision GNSS for everyone. *GPS World*, 27(11), 43–48.
- Basiri, A., Amirian, P., & Mooney, P. (2016). Using crowdsourced trajectories for automated OSM data entry approach. *Sensors*, 16(9), 1510. <https://doi.org/10.3390/s16091510>.
- Biljecki, F., Ledoux, H., & Stoter, J. (2017). Generating 3D city models without elevation data. *Computers, Environment and Urban Systems*, 64, 1–18. <https://doi.org/10.1016/j.compenvurbysys.2017.01.001>.
- Biljecki, F., et al. (2015). Applications of 3D city models: State of the art review. *ISPRS International Journal of Geo-Information*, 4(4), 2842–2889. <https://doi.org/10.3390/ijgi4042842>.
- Biljecki, F., et al. (2016). The variants of an LOD of a 3D building model and their influence on spatial analyses. *ISPRS Journal of Photogrammetry and Remote Sensing*, 116, 42–54. <https://doi.org/10.1016/j.isprsjprs.2016.03.003>.
- Blum, A., & Mitchell, T. (1998). Combining labeled and unlabeled data with co-training. In *Proceedings of the eleventh annual conference on Computational learning theory* (pp. 92–100).
- Bourdeau, A., Sahnoudi, M., & Tournet, J. Y. (2012). Tight integration of GNSS and a 3D city model for robust positioning in urban canyons. In *Proceedings of the 25th international technical meeting of the satellite division of the institute of navigation (ION GNSS 2012)* (pp. 1263–1269).

- Bradbury, J. (2007). Prediction of urban GNSS availability and signal degradation using virtual reality city models. In *Proceedings of the 20th international technical meeting of the satellite division of the institute of navigation (ION GNSS 2007)* (pp. 2696–2706).
- Breßler, J., et al. (2016). GNSS positioning in non-line-of-sight context—A survey. In *2016 IEEE 19th international conference on intelligent transportation systems (ITSC)* (pp. 1147–1154). IEEE. <https://doi.org/10.1109/ITSC.2016.7795701>.
- Broadhurst, A., Drummond, T. W., & Cipolla, R. (2001). A probabilistic framework for space carving. In *1. Proceedings eighth IEEE international conference on computer vision. ICCV 2001* (pp. 388–393). IEEE. <https://doi.org/10.1109/ICCV.2001.937544>.
- Chen, X., et al. (2012). *Antennas for global navigation satellite systems*. John Wiley & Sons. <https://doi.org/10.1002/9781119969518>. Chap. 8.
- Cyganek, B., & Paul Siebert, J. (2009). *An introduction to 3D computer vision techniques and algorithms*. John Wiley & Sons. <https://doi.org/10.1002/9780470699720>.
- Dinse, G. E. (2011). An EM algorithm for fitting a four-parameter logistic model to binary dose-response data. *Journal of Agricultural, Biological, and Environmental Statistics*, 16, 221–232. <https://doi.org/10.1007/s13253-010-0045-3>.
- Döllner, J., et al. (2006). The virtual 3d city model of berlin—managing, integrating, and communicating complex urban information. In *Proceedings of the 25th international symposium on urban data management UDMS 2006 in Aalborg, Denmark, 15–17 May 2006*.
- Dukai, B., Ledoux, H., & Stoter, J. E. (2019). A multi-height LoD1 model of all buildings in the Netherlands. In *ISPRS annals of photogrammetry, remote sensing and spatial information sciences 4.4/W8* (pp. 51–57). <https://doi.org/10.5194/isprs-annals-4-4-W8-51-2019>.
- European Global Navigation Satellite Systems Agency. (2017). *White Paper on using GNSS Raw Measurements on Android devices*. <https://www.euspa.europa.eu/newsroom/news/available-now-white-paper-using-gnss-raw-measurements-android-devices>. Access Feb 2021.
- European Global Navigation Satellite Systems Agency. (2020). *GNSS User Technology Report*. European Global Navigation Satellite Systems Agency.
- Fan, H., et al. (2014). Quality assessment for building footprints data on OpenStreetMap. *International Journal of Geographical Information Science*, 28(4), 700–719. <https://doi.org/10.1080/13658816.2013.867495>.
- Floreano, D., & Wood, R. J. (2015). Science, technology and the future of small autonomous drones. *Nature*, 521(7553), 460–466. <https://doi.org/10.1038/nature14542>.
- Furukawa, Y., & Hernández, C. (2015). Multi-view stereo: A tutorial. In *9. Foundations and Trends® in computer graphics and vision* (pp. 1–148). <https://doi.org/10.1561/0600000052>, 1–2.
- Girindran, R., et al. (2020). On the reliable generation of 3D city models from open data. *Urban Science*, 4(4), 47. <https://doi.org/10.3390/urbansci4040047>.
- Goetz, M. (2013). Towards generating highly detailed 3D CityGML models from OpenStreetMap. *International Journal of Geographical Information Science*, 27(5), 845–865. <https://doi.org/10.1080/13658816.2012.721552>.
- Google. (2020). Google Earth Pro 7.3.3.7786 [Computer software]. Elevation profile of paths at UCL (51.52474621074047°N, 0.1337747536514156°W to 51.524661482298853°N, 0.1336670761779679°W), Goodchild Road (51.57049612210949°N, 0.0908854920709079°W to 51.57025545560245°N, 0.09081501658615987°W), and Hermitage Road (51.57498848871381°N, 0.09731098311117847°W to 51.57497270042291°N, 0.09726613066514123°). url: <https://www.google.com/earth/index.html> (visited on 03/15/2021).
- Groves, P. D., & Jiang, Z. (2013). Height aiding, C/N0 weighting and consistency checking for GNSS NLOS and multipath mitigation in urban areas. *The Journal of Navigation*, 66(5), 653–669. <https://doi.org/10.1017/S0373463313000350>.
- Groves, P. D., et al. (2012). Intelligent urban positioning using multi-constellation GNSS with 3D mapping and NLOS signal detection. In *Proceedings of the 25th international technical meeting of the satellite division of the institute of navigation (ION GNSS 2012)* (pp. 458–472).
- Groves, P. D., et al. (2013). A portfolio approach to NLOS and multipath mitigation in dense urban areas. In *Proceedings of the 26th international technical meeting of the satellite division of the institute of navigation (ION GNSS+ 2013)* (pp. 3231–3247).
- Healy, M. J. R. (1972). Statistical analysis of radioimmunoassay data. *Biochemical Journal*, 130(1), 207–210.
- Hsu, L.-T. (2017). GNSS multipath detection using a machine learning approach. In *2017 IEEE 20th international conference on intelligent transportation systems (ITSC)* (pp. 1–6). IEEE. <https://doi.org/10.1109/ITSC.2017.8317700>.
- Huang, R., et al. (2013). Evaluation of GPS trajectories on VGI and social websites. In *2013 21st international conference on geoinformatics* (pp. 1–5). IEEE. <https://doi.org/10.1109/GeoInformatics.2013.6626121>.
- International Data Corporation. (2020). Smartphone market share. url: <https://www.idc.com/promo/smartphone-market-share/os.html> (visited on 10/12/2020).
- Irish, A. T., et al. (2014a). Belief propagation based localization and mapping using sparsely sampled GNSS SNR measurements. In *2014 IEEE international conference on robotics and automation (ICRA)* (pp. 1977–1982). IEEE. <https://doi.org/10.1109/ICRA.2014.6907121>.
- Irish, A. T., et al. (2014b). Probabilistic 3D mapping based on GNSS SNR measurements. In *2014 IEEE international conference on acoustics, speech and signal processing (ICASSP)* (pp. 2390–2394). IEEE. <https://doi.org/10.1109/ICASSP.2014.6854028>.
- Isaacs, J. T., et al. (2014). Bayesian localization and mapping using GNSS SNR measurements. In *2014 IEEE/ION position, location and navigation symposium-PLANS 2014* (pp. 445–451). IEEE. <https://doi.org/10.1109/PLANS.2014.6851402>.
- Jiang, Z., & Groves, P. D. (2012). GNSS NLOS and multipath error mitigation using advanced multi-constellation consistency checking with height aiding. In *Proceedings of the 25th international technical meeting of the satellite division of the institute of navigation (ION GNSS 2012)* (pp. 79–88).

- Jiang, Z., et al. (2011). Multi-constellation GNSS multipath mitigation using consistency checking. In *Proceedings of the 24th international technical meeting of the satellite division of the institute of navigation (ION GNSS 2011)* (pp. 3889–3902). Institute of Navigation.
- Kim, K., et al. (2008). Localization and 3D reconstruction of urban scenes using GPS. In *2008 12th IEEE international symposium on wearable computers* (pp. 11–14). IEEE. <https://doi.org/10.1109/ISWC.2008.4911576>.
- Kintner, P. M., Humphreys, T., & Hinks, J. (2009). GNSS and ionospheric scintillation. *Inside GNSS*, 4(4), 22–30.
- Kolbe, T. H. (2009). Representing and exchanging 3D city models with CityGML. In J. Lee, & S. Zlatanova (Eds.), *3D geo-information sciences* (pp. 15–31). Springer. https://doi.org/10.1007/978-3-540-87395-2_2.
- Kolbe, T. H., Gröger, G., & Plümer, L. (2008). CityGML–3D city models and their potential for emergency response. In S. Zlatanova, & J. Li (Eds.), *Geospatial information technology for emergency response* (pp. 257–274). Taylor & Francis. <https://doi.org/10.4324/9780203928813>.
- Kutulakos, K. N., & Seitz, S. M. (1999). A theory of shape by space carving. In *1. Proceedings of the seventh IEEE international conference on computer vision* (pp. 307–314). IEEE. <https://doi.org/10.1109/ICCV.1999.791235>.
- Lafarge, F., & Mallet, C. (2012). Creating large-scale city models from 3D-point clouds: A robust approach with hybrid representation. *International Journal of Computer Vision*, 99, 69–85. <https://doi.org/10.1007/s11263-012-0517-8>.
- Langley, R. B., Teunissen, P. J. G., & Montenbruck, O. (2017). Introduction to GNSS. In P. J. Teunissen, & O. Montenbruck (Eds.), *Springer handbook of global navigation satellite systems* (pp. 3–23). Springer. https://doi.org/10.1007/978-3-319-42928-1_1.
- Levinson, J., et al. (2011). Towards fully autonomous driving: Systems and algorithms. In *2011 IEEE intelligent vehicles symposium (IV)* (pp. 163–168). IEEE. <https://doi.org/10.1109/IVS.2011.5940562>.
- Lin, H., et al. (2009). A virtual geographic environment for a simulation of air pollution dispersion in the pearl river delta (PRD) region. In J. Lee, & S. Zlatanova (Eds.), *3D geo-information sciences* (pp. 15–31). Springer. https://doi.org/10.1007/978-3-540-87395-2_1.
- Liu, S., & Cooper, D. B. (2011). A complete statistical inverse ray tracing approach to multi-view stereo. In *CVPR 2011* (pp. 913–920). IEEE. <https://doi.org/10.1109/CVPR.2011.5995334>.
- Mayer, V., et al. (2019). ESA multi-GNSS products. In *21. Geophysical research abstracts*. EGU General Assembly.
- Molisch, A. F. (2011). *Wireless communications*. John Wiley & Sons.
- Möller, G., & Landskron, D. (2019). Atmospheric bending effects in GNSS tomography. *Atmospheric Measurement Techniques*, 12(1), 23–34. <https://doi.org/10.5194/amt-12-23-2019>.
- Obst, M., Bauer, S., & Wanielik, G. (2012). Urban multipath detection and mitigation with dynamic 3D maps for reliable land vehicle localization. In *Proceedings of the 2012 IEEE/ION position, location and navigation symposium* (pp. 685–691). IEEE. <https://doi.org/10.1109/PLANS.2012.6236944>.
- Open Geospatial Consortium. (2012). *Public Engineering Report (OGC 12-075)*. In Arne Schilling, Benjamin Hagedorn, & Volker Coors (Eds.). http://www.opengis.net/doc/ie/3dpie_12-075_OGC_3DPIE_Final_Report.pdf, Access Feb 2021.
- Ordnance Survey. (2020a). *A guide to coordinate systems in Great Britain*. Ordnance Survey.
- Ordnance Survey. (2020b). OS MasterMap building height attribute. Using: EDINA digimap ordnance survey service. url: <http://edina.ac.uk/digimap> (visited on 10/2020).
- Ordnance Survey. (2020c). OS mastermap topography layer. Using: EDINA digimap ordnance survey service. url: <http://edina.ac.uk/digimap> (visited on 10/2020).
- Ordnance Survey. (2020d). OS terrain 5 DTM. Using: EDINA digimap ordnance survey service. url: <http://edina.ac.uk/digimap> (visited on 10/2020).
- Peyraud, S., et al. (2013). About non-line-of-sight satellite detection and exclusion in a 3D map-aided localization algorithm. *Sensors*, 13(1), 829–847. <https://doi.org/10.3390/s130100829>.
- Pu, S., & Vosselman, G. (2006). Automatic extraction of building features from terrestrial laser scanning. *The International Archives of the Photogrammetry, Remote Sensing and Spatial Information Sciences*, 36(5), 25–27.
- Pu, S., & Zlatanova, S. (2005). Evacuation route calculation of inner buildings. In *Geo-information for disaster management* (pp. 1143–1161). Springer. https://doi.org/10.1007/3-540-27468-5_79.
- Remondino, F., & El-Hakim, S. (2006). Image-based 3D modelling: A review. *The Photogrammetric Record*, 21(115), 269–291. <https://doi.org/10.1111/j.1477-9730.2006.00383.x>.
- Rodrigues, J. G. P., & Aguiar, A. (2019). Extracting 3D maps from crowdsourced GNSS Skyview data. In *The 25th annual international conference on mobile computing and networking* (p. 115).
- Ruder, S. (2016). An overview of gradient descent optimization algorithms. *arXiv preprint*. arXiv:1609.04747.
- Salk, C. F., et al. (2016). Assessing quality of volunteer crowdsourcing contributions: Lessons from the cropland capture game. *International Journal of Digital Earth*, 9(4), 410–426. <https://doi.org/10.1080/17538947.2015.1039609>.
- Seitz, S. M., et al. (2006). A comparison and evaluation of multi-view stereo reconstruction algorithms. In *2006 IEEE computer society conference on computer vision and pattern recognition (CVPR'06)* (pp. 519–528). IEEE. <https://doi.org/10.1109/CVPR.2006.19>.
- Snaveley, N., Seitz, S. M., & Szeliski, R. (2008). Modeling the world from internet photo collections. *International Journal of Computer Vision*, 80(2), 189–210.
- Soloviev, A., & Van Graas, F. (2009). Use of deeply integrated GPS/INS architecture and laser scanners for the identification of multipath reflections in urban environments. *IEEE Journal of Selected Topics in Signal Processing*, 3(5), 786–797. <https://doi.org/10.1109/JSTSP.2009.2027796>.
- Steigenberger, P., Thöelert, S., & Montenbruck, O. (2018). GNSS satellite transmit power and its impact on orbit determination. *Journal of Geodesy*, 92, 609–624. <https://doi.org/10.1007/s00190-017-1082-2>.
- Subirana, J. S., Zornoza, J. M. J., & Hernández-Pajares, M. (2013). *Gnss data processing volume 1: Fundamentals and algorithms*. ESA Communications.
- Suveg, Ildiko and George Vosselman (2004). "Reconstruction of 3D building models from aerial images and maps". In: ISPRS Journal of Photogrammetry and remote sensing 58.3–4, pp. 202–224. doi: <https://doi.org/10.1016/j.isprsjprs.2003.09.006>.
- Swinford, R. P. (2005). Building on-the-fly world models for pervasive gaming and other ubicomp applications using GPS availability data. In *The IEEE international workshop on intelligent environments, 2005* (pp. 133–142). IET. <https://doi.org/10.1049/ic:20050227>.
- Verbree, E., & Zlatanova, S. (2007). Positioning LBS to the third dimension. In G. Gartner, W. Cartwright, & M. P. Peterson (Eds.), *Location based services and telecartography* (pp. 107–118). Springer. https://doi.org/10.1007/978-3-540-36728-4_8.
- Wang, L., Groves, P. D., & Ziebart, M. K. (2013). GNSS shadow matching: Improving urban positioning accuracy using a 3D city model with optimized visibility scoring scheme. *Navigation: Journal of the Institute of Navigation*, 60(3), 195–207. <https://doi.org/10.1002/navi.38>.
- Wang, L., Groves, P. D., & Ziebart, M. K. (2015). Smartphone shadow matching for better cross-street GNSS positioning in urban environments. *The Journal of Navigation*, 68(3), 411–433. <https://doi.org/10.1017/S0373463314000836>.
- Weissman, A., et al. (2013). 2.5 D mapping using GNSS signal analysis. In *2013 10th workshop on positioning, navigation and communication (WPNC)* (pp. 1–6). IEEE. <https://doi.org/10.1109/WPNC.2013.6533290>.
- Xu, H., et al. (2018). GNSS shadow matching based on intelligent LOS/NLOS classifier. In *The 16th world congress of the international association of institutes of navigation (IAIN) Chiba, Japan*. IAIN.
- Xu, H., et al. (2020). Machine learning based LOS/NLOS classifier and robust estimator for GNSS shadow matching. *Satellite Navigation*, 1, 1–12. <https://doi.org/10.1186/s43020-020-00016-w>.
- Yin, X., Wonka, P., & Razdan, A. (2008). Generating 3d building models from architectural drawings: A survey. *IEEE Computer Graphics and Applications*, 29(1), 20–30. <https://doi.org/10.1109/MCG.2009.9>.
- Yozevitch, R., Ben-Moshe, B., & Dvir, A. (2014). GNSS accuracy improvement using rapid shadow transitions. *IEEE Transactions on Intelligent Transportation Systems*, 15(3), 1113–1122. <https://doi.org/10.1109/ITITS.2013.2294537>.
- Yozevitch, R., Moshe, B. B., & Weissman, A. (2016). A robust GNSS los/nlos signal classifier. *NAVIGATION: Journal of The Institute of Navigation*, 63(4), 429–442. <https://doi.org/10.1002/navi.166>.
- Zebedin, L., et al. (2006). Towards 3D map generation from digital aerial images. *ISPRS Journal of Photogrammetry and Remote Sensing*, 60(6), 413–427. <https://doi.org/10.1016/j.isprsjprs.2006.06.005>.